Design of a calorimeter for near-field heat transfer measurements and thermal scanning probe microscopy

Bijster, R. J.F.; Van Keulen, F.

Important note
To cite this publication, please use the final published version (if applicable).
Please check the document version above.

Design of a calorimeter for near-field heat transfer measurements and thermal scanning probe microscopy

R. J. F. Bijster, and F. van Keulen

View Online **Export Citation** **CrossMark**

AIP Publishing

Design of a calorimeter for near-field heat transfer measurements and thermal scanning probe microscopy

View Online   Export Citation   CrossMark

R. J. F. Bijster[1,2,a] (iD) and F. van Keulen[1] (iD)

AFFILIATIONS

[1] Department of Precision and Microsystems Engineering, Delft University of Technology, 2628 CD Delft, The Netherlands
[2] Department of Optomechatronics, TNO, Stieltjesweg 1, 2628 CK Delft, The Netherlands

[a] Author to whom correspondence should be addressed: r.j.f.bijster@tudelft.nl

ABSTRACT

Multilayer cantilever beams are used in the measurement of near-field radiative heat transfer. The materials and dimensions of the cantilever probe are chosen in order to improve system performance in terms of sensitivity and noise. This is done using an analytical model that describes the thermo-mechanical and mechanical behavior of the cantilever and its influences at the system level. In the design, the optical reflectance and the sensitivity of cantilever rotation to the heat input are maximized under constraints for thermal noise, temperature drift, and a lower bound for the spring constant. The analytical model is verified using finite element analysis, which shows that the effects of radiative losses to the environment are insignificant for design purposes, while the effects of ignoring three-dimensional heat flow introduces larger errors. Moreover, the finite element analysis shows that the designed probes are up to 41 times more sensitive than the often used commercial-of-the-shelf benchmark and have a four times lower thermal noise. Experimental validation of the designed probes shows good agreement with the theoretical values for sensitivity. However, the most sensitive designs were found to be susceptible to damage due to overheating and carbon contamination.

Published under license by AIP Publishing. https://doi.org/10.1063/5.0034503

I. INTRODUCTION

In 1969, Hargreaves[1] published a seminal paper on what he called "anomalous radiative transfer between closely spaced bodies." His measurements confirmed the predictions of Rytov's theory of fluctuational electrodynamics,[2,3] which were later further developed by Polder and Van Hove.[4] This effect, in which the heat flux increases rapidly with diminishing separations and exceeds the black-body limit due to near-field effects, has since then been observed and quantified by several research groups. The measurement systems employed for this measurement can be roughly classified into three archetypes: (1) two closely spaced parallel plates in which one plate is kept at a constant temperature, while the temperature of the other is measured as a function of their separation;[5–24] (2) a miniature thermocouple scanning over a surface in which the temperature of the tip is measured as a function of separation;[25–31] and (3) a thermo-mechanical probe scanning over a surface in which the deformation of the probe is used to determine the probe temperature or the heat flux.[32–37]

Closely spaced parallel plates are ideal to mimic the conditions described in theoretical work and can be used to study applications such as thermophotovoltaics and photonic cooling.[22] They benefit from large interacting surfaces and the associated larger signals. In general, however, the required degree of parallelism is difficult to obtain at smaller separations. Miniature thermocouples and thermo-mechanical probes are generally easier to implement experimentally and can measure local variations in the thermal conductance. Moreover, probe-based techniques are less sensitive to alignment errors at smaller separations than parallel plates and offer shorter response times due to the smaller thermal capacitance of the probes. This allows their use for applications in scanning probe microscopy. The sensitive area of probes with integrated thermocouples is typically very small, making them suitable for thermal scanning probe microscopy applications with high spatial resolution.

Heating elements are easily integrated in the probe during manufacturing. The thermo-mechanical probes, however, can be simple to manufacture and require no additional patterning steps. The size of the interacting area and its material can be tuned after manufacturing of the probe by attaching different sizes of spheres. As no heating elements are typically integrated in the probe, the temperature needs to be controlled by external means, and the achievable performance has a greater interaction with the supporting systems.

When using a thermo-mechanical probe, a glass microsphere is attached to the free-end of a multilayer probe. The heat transfer occurs between the sphere and the sample, while the probe is used as a transducer. Because the layers expand at distinct rates, the thermal load results in a mechanical deformation, which can be measured using the optical beam deflection (OBD) method.[38] In this method, light is reflected off the reflective coating of the probe onto a position sensitive detector (PSD). The local rotation of the probe results in a shift of the spot on the PSD, as is shown schematically in Fig. 1. In many instances, a probe with a triangular plan form, silicon-nitride base, and a gold reflective coating on one side is used. From the commercially available options, Wanders[39] identified the Bruker/Veeco MLCT-C probe as one of the most sensitive options for this specific measurement. Others have used very similar probes by other manufacturers, which are very comparable in terms of the dimensions and used materials.[32–34]

When considering the entire measurement system, the sensitivity of the output signal of the PSD as the result of a flux P absorbed at the tip of the probe can be written as

$$\frac{\partial X_p}{\partial P} = \frac{\partial X_p}{\partial x} \frac{\partial x}{\partial \theta} \frac{\partial \theta}{\partial P}, \tag{1}$$

where X_p is the output of the PSD, x is the location of the spot on the PSD, and θ is the (local) rotation of the cantilever. While the first two terms, $\partial X_p/\partial x$ and $\partial x/\partial \theta$, are specific to the design of the OBD system, the sensitivity $\partial \theta/\partial P$ can be designed separately by choosing the materials and dimensions of the cantilever.

Commercially available probes are not optimized for use as thermo-mechanical transducers. Probes that are designed specifically for this purpose can have a higher sensitivity and improved noise performance. Moreover, the performance of the measurement system can be improved further by considering the probe as an integral part of the system. For example, the sensitivity $\partial X_p/\partial x$ is directly proportional to the intensity of the light incident on the PSD. This intensity is affected by the reflectance of the probe. Therefore, there is a need for cantilever probes that are designed for the particular purpose of measuring heat transfer at small separations and for which the interrelations with the measurement system are considered.
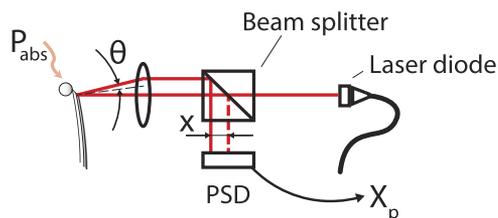
Bilayer cantilever probes have previously been designed and optimized for calorimetry applications with picowatt and femtojoule resolutions.[40–42] However, these designs consider only the cantilevers and the lock-in techniques used to measure their behavior. They do not consider the steady-state performance or the interrelations between the cantilever design and system performance. Moreover, they do not consider the presence of a microsphere at the free-end of the cantilever either.

In this paper, cantilever probe designs are presented that are dedicated to measuring near-field radiative heat transfer under vacuum conditions. In contrast to the previous designs of thermo-mechanical probes, the optical contribution of the probe to the measurement system is taken into account, as well as thermal drift of the clamp. Moreover, the effects of the microsphere are considered. The designed probes have been manufactured and are benchmarked numerically and experimentally against the Bruker MLCT-C. The resulting cantilever probes are shown numerically and experimentally to have significantly improved performance compared to the benchmark.

II. DESIGNING THE CANTILEVER

The dimensions of the cantilever as used throughout this paper are schematically indicated in Fig. 2. The layer thicknesses t_i, the width w, and the length L are chosen under multiple design constraints. A sphere is attached to the free-end of the cantilever, which is perpendicular to the sample. The sphere and the sample are separated by a distance g.

The sensitivity of the probe can be written as

$$\frac{\partial \theta}{\partial P} = \frac{L^2}{wt_2^2}\Gamma, \tag{2}$$

where Γ is in an auxiliary term (unit of W^{-1}) that contains the relevant material properties and the ratio of layer thicknesses h,

$$\Gamma = \frac{3hm\Delta\alpha}{hk_1 + k_2}\left(\frac{1+h}{1 + 2hm(2 + 3h + 2h^2) + h^4m^2}\right), \tag{3}$$

where $h = t_1/t_2$, $m = M_1/M_2$, $M_i = E_i/(1 - v_i)$, and $\Delta\alpha = \alpha_1 - \alpha_2$ is the difference in the coefficients of thermal expansion. In this relation, E_i and v_i are the Young's modulus and the corresponding Poisson ratio for layer i, and k_i is the associated thermal conductivity.

FIG. 1. Schematic representation of a confocal optical beam deflection system. A laser beam is reflected off a rotated cantilever. Through a lens, the rotation of the beam is translated into a shift on the position sensitive detector.
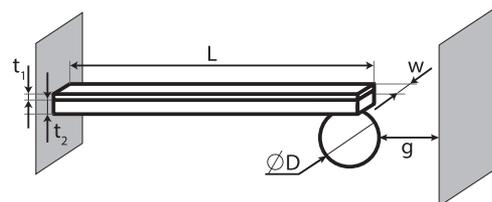
FIG. 2. Schematic representation of calorimeter consisting of a bilayer cantilever that is clamped at one end and has a microsphere at its free-end. The relevant dimensions of length, width, and thicknesses are indicated. The subscripts 1 and 2 refer to the reflective coating and the substrate, respectively.

TABLE I. Complex refractive indices at a wavelength λ = 635 nm for the studied thin films.

Material	Refractive index	Source
Gold, Au	0.180 16 + 3.453 1i	Johnson and Christy[46,47]
Aluminum, Al	1.462 2 + 7.559 2i	Rakić[47,48]
Silicon, Si	3.878 7 + 0.019 221i	Aspnes and Studna[47,49]
Silicon nitride, Si₃N₄	2.022	Filmetrics[50]
Silicon dioxide, SiO₂	1.457	Malitson[51]
Silicon carbide, SiC	2.635	Filmetrics[52]

The derivation of these equations is provided in the supplementary material.

From Eqs. (2) and (3), it follows that the parameter L^2/w, the layer thickness t_2 (or t_1), and the thickness ratio h (through Γ) can be chosen independently to tune the sensitivity of the probe.

A. Choosing the layer thicknesses

The layer thicknesses tie into two parameters of the system sensitivity given by Eq. (1): the sensitivity of the PSD signal to beam shift $\partial X_\text{p}/\partial x$ and the sensitivity of cantilever rotation to absorbed power $\partial\theta/\partial P$. The former is directly proportional to the amount of reflected light and benefits from a high reflectivity of the cantilever.[43] The reflectivity is predominantly determined by the thickness of the coating and is very sensitive to thickness variations at thin layers. The sensitivity $\partial\theta/\partial P$, on the other hand, can be tuned by other parameters. For these reasons, a two-step approach is chosen in which the minimum layer thickness is determined that maximizes the reflectance and that is robust against the small variations in thickness that arise from manufacturing tolerances. The thickness ratio h is chosen separately to maximize Γ. Combined, these yield the required substrate thickness.

1. Coating thickness for maximum reflectance

To determine the required coating thickness for maximum reflectance, the cantilever is modeled as a one-dimensional stratified medium consisting of a (thin) reflective coating on top of a (thick) substrate. Using the Fresnel equations and the Transfer Matrix Method (TMM),[44,45] the reflectance and transmittance of this structure are calculated. The absorptance then follows from conservation of energy. The values for the complex refractive indices ($n = n'$ + iκ) of the considered materials are listed in Table I for a wavelength of λ = 635 nm.

The results of the TMM simulation for eight material combinations are shown in Figs. 3–5. The combinations consist of a gold or aluminum coating on top of a silicon, silicon dioxide, silicon nitride, or silicon carbide substrate. Furthermore, the thickness ratios 0.1, 0.25, and 0.5 are considered for each combination.

In all cases, two clear branches can be distinguished as soon as bulk properties are attained. In that case, a gold coating outperforms an aluminum coating in terms of reflectance at equal thickness and equal thickness ratio. Moreover, as soon as bulk properties are attained, the substrate material becomes inconsequential for the reflectance.

For a gold coating, the reflectance is independent of the layer thickness for $t_1 \geq 110$ nm irrespective of the thickness ratio. Although almost similar reflectance can be obtained for lower thicknesses, the results are less robust against manufacturing errors due to (strong) local dips in the reflectance at lower thickness ratios.

For aluminum coatings and thickness ratios of 0.25 and 0.5, a coating thickness of 35 nm on top of a silicon substrate suffices to attain a reflectance that is independent of coating thickness. For the lower thickness ratio of 0.1, a minimum coating thickness of 50 nm is required for the same effect.

2. Choosing the thickness ratio

A high sensitivity is attained by maximizing the parameter Γ, which is plotted as a function of the thickness ratio h in Fig. 6. It is important to note that similar to Lai et al.,[41] the thickness ratio h
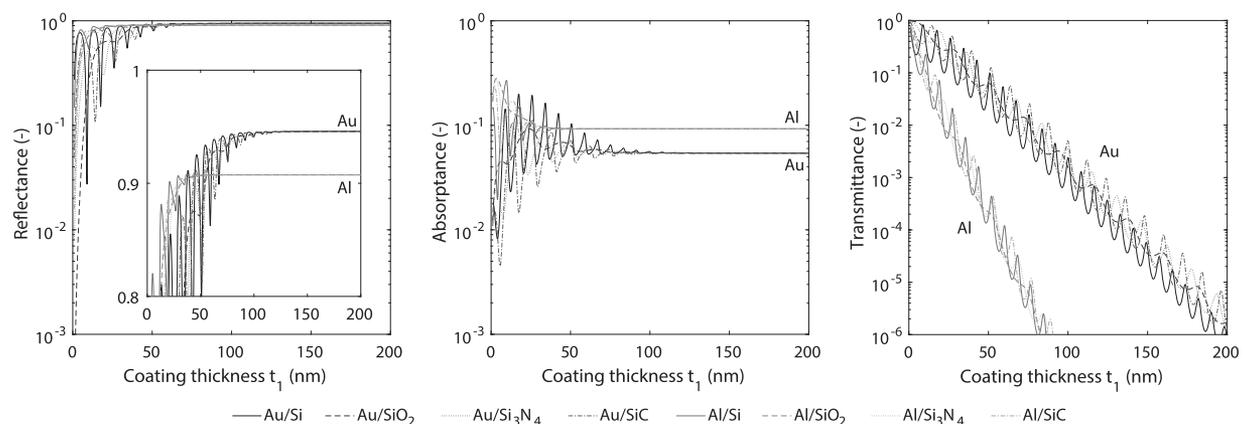
FIG. 3. Absorptance, transmittance, and reflectance for different coating and substrate combinations (thickness ratio h = 0.1).
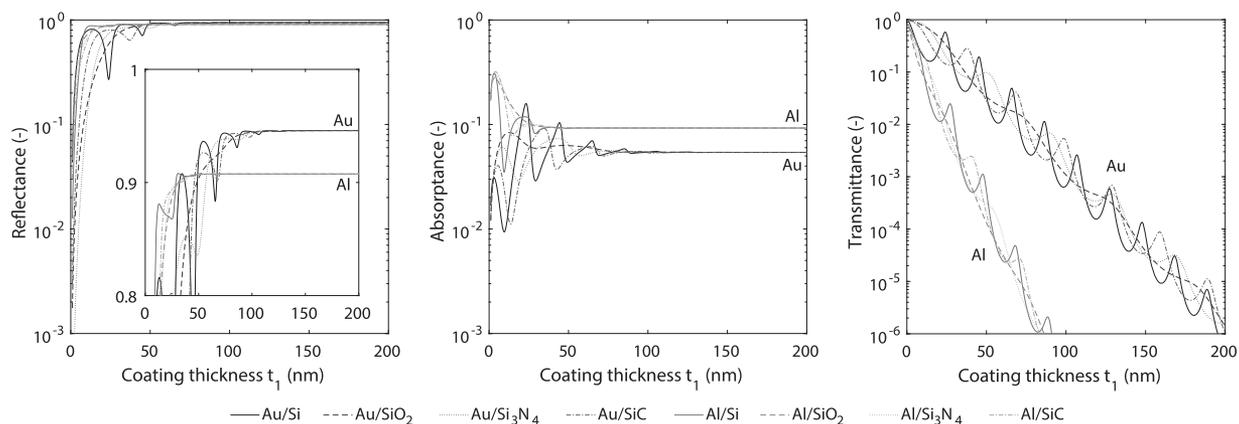
FIG. 4. Absorptance, transmittance, and reflectance for different coating and substrate combinations (thickness ratio h = 0.25).

is found under the assumption that the material properties are independent of film thickness. The validity of this assumption is moot, as, in practice, these effective material properties can be strongly dependent on film thickness before reaching the bulk values (see, e.g., the work of Abazari et al.[53] for the case of the elastic modulus). However, processing conditions seem to be equally, if not more, important contributors to the *effective* material parameters[54] and can vary with processing parameters from foundry to foundry. Because accurate data on the relation between material properties and the layer thickness are unavailable, the bulk values or the generally accepted values for thin films are used for this design. The used values are listed in Table II.

For all thickness ratios of practical interest ($h \leq 1$), combinations with an aluminum coating perform significantly better than the gold-coated counterparts. This is a direct consequence of the higher coefficient of thermal expansion of aluminum. The values of Γ are highest for combinations with a silicon dioxide substrate. However, the Young's modulus of SiO$_2$ is significantly lower than that of Si$_3$N$_4$ and SiC, making them comparatively compliant at equal h. To

illustrate this, the spring constant C of the cantilevers is written as

$$C = \frac{3EI}{L^3} = \frac{wt^3}{4L^3}\Psi,$$ (4)

with $t_2 = \frac{t}{1+h}$, $t = t_1 + t_2$, and Ψ being

$$\Psi = \frac{hE_1E_2}{(1+h)^3(hE_1+E_2)}\left(4 + 6h + 4h^2 + \frac{E_1}{E_2}h^3 + \frac{E_2}{E_1}\frac{1}{h}\right).$$ (5)

This effective Young's modulus is shown as a function of the thickness ratio in Fig. 7. At the equal thickness ratio h, combinations with a Si$_3$N$_4$ substrate are up to 4.2 times stiffer than the SiO$_2$ alternatives. To achieve a practical bending stiffness, a silicon nitride substrate with an aluminum coating was selected as the next best alternative.
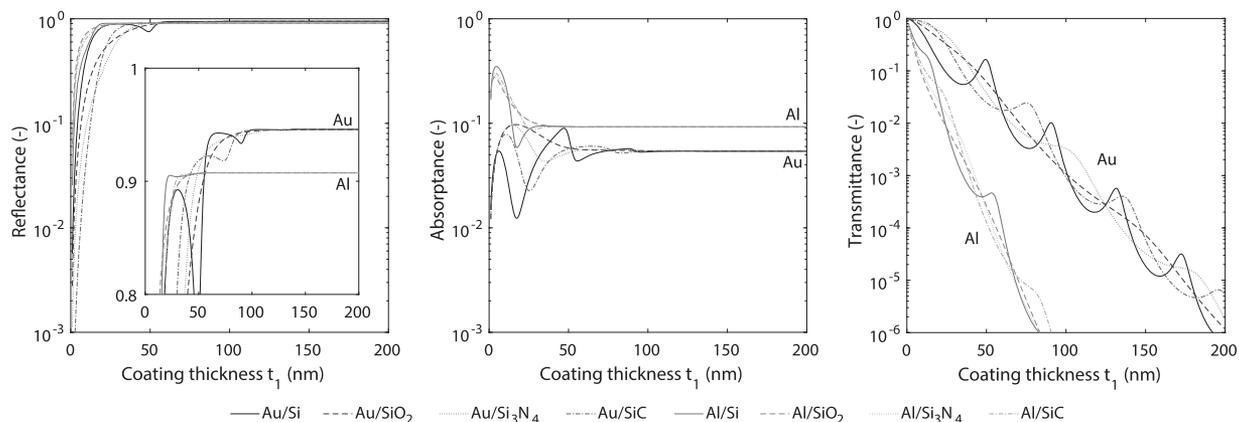
FIG. 5. Absorptance, transmittance, and reflectance for different coating and substrate combinations (thickness ratio h = 0.5).
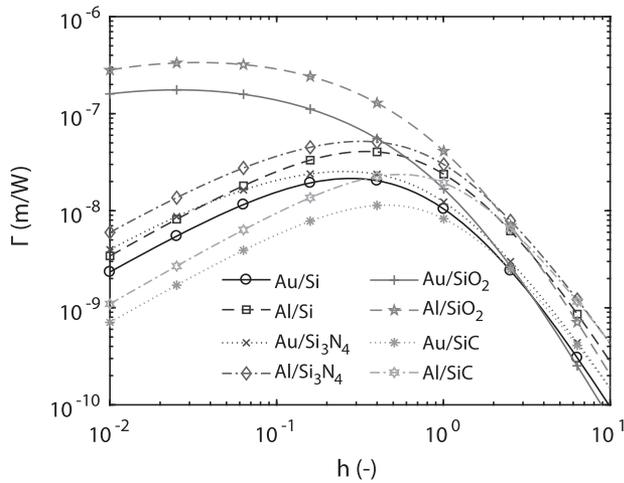
FIG. 6. Auxiliary term Γ for the rotation of a cantilever beam at its tip as a function of $h = t_1/t_2$. Note: markers do not correspond to data but are used to identify the lines.

FIG. 7. Effective Young's modulus Ψ as a function of the ratio of layer thicknesses $h = t_1/t_2$. In all cases, Ψ is dominated by the choice in the substrate material. The choice for a coating material is of little influence in comparison. Note: markers do not correspond to data but are used to identify the lines.

A coating thickness of t_1 = 100 nm was used to ensure a sufficiently stiff cantilever with an optical performance that is robust against small variations in the layer thicknesses. With Γ at its maximum value for this combination at $h \approx 0.32$, it follows that t_2 = 310 nm.

B. Choosing the length and width

Following Eq. (2), the sensitivity $\frac{\partial \theta}{\partial P}$ follows from appropriate values for the length and width of the cantilever, as well as the thickness of the substrate. The aspect ratio of the cantilever is constrained by the performance of the optical beam deflection system and the data-acquisition system (DAQ) and the requirements on resolution, noise contributions, and spring stiffness.

As per Eq. (1), the sensitivity of the OBD is the product of the three sensitivities $\partial X_p/\partial x$, $\partial x/\partial \theta$, and $\partial \theta/\partial P(L)$. The first two are determined in the optical design and are limited by the practical limitations of the available hardware. The latter is set by the cantilever according to Eq. (2). The smallest detectable change in the output potential of the PSD is

$$\Delta U_{\mathrm{DAQ}} = \frac{U_{\mathrm{range}}}{2^{n_{\mathrm{bits}}}}, \tag{6}$$

where U_{range} is the full range of the data-acquisition system and n_{bits} is the (effective) number of bits available in the analog-to-digital converter. From this, the required value of $\partial X_p/\partial P$ is obtained as

$$\left.\frac{\partial X_p}{\partial P}\right|_{\mathrm{reqt}} = \frac{\Delta U_{\mathrm{DAQ}}}{\Delta P_{\mathrm{resolution}}}, \tag{7}$$

where $\Delta P_{\mathrm{resolution}}$ is the required static resolution of the calorimeter. The corresponding sensitivity of the cantilever is then obtained as

$$\left.\frac{\partial \theta}{\partial P}\right|_{\mathrm{reqt}} = \left.\frac{\partial X_p}{\partial P}\right|_{\mathrm{reqt}} \left(\frac{\partial X_p}{\partial x}\frac{\partial x}{\partial \theta}\right)^{-1}. \tag{8}$$

To create an envelope that is bounded by the design constraints, the constraints are written as functions of the form L^n/w. For the required sensitivity of Eq. (2), this can be rewritten as

$$\frac{L^2}{w} = \frac{t_2^2}{\Gamma}\left.\frac{\partial \theta}{\partial P}\right|_{\mathrm{reqt}} \tag{9}$$

and imposes a lower limit on L^2/w. Additional constraints are imposed by the thermal noise and the sensitivity to fluctuations in the base temperature.

The temperature of the cantilever clamp will, in practice, drift over time and will be known with limited accuracy. A change in temperature at the clamped-end of the cantilever (the base) ΔT_{base} affects the temperature distribution over the entire cantilever length and thus the cantilever rotation and deflection. With the OBD method, this effect and the effect of a heat input at the free-end of the cantilever cannot be distinguished. The corresponding uncertainty in the measured thermal input can be written as the product of the uncertainty in the clamp temperature ΔT_{base} and the conductance G,

$$\left.\Delta \hat{P}\right|_{\Delta T_{\mathrm{base}}} = 2G\Delta T_{\mathrm{base}}. \tag{10}$$

TABLE II. Material properties used for optimization of the cantilever dimensions.

Property	Au[55]	Si[56]	Al[57]	Si$_3$N$_4$	SiO$_2$[58]	SiC[59]
E (GPa)	77.2	112.4	68	280[60,61]	66	410
$\nu(-)$	0.42	0.28	0.36	0.20[60,61]	0.17	0.14
k (W m^{-1} K^{-1})	301	124	210	30.1[62]	1.1	120
α (ppm/K)	14.4	2.5	24	2.8	0.56	4
ρ (kg m^{-3})	19 320	2329	2699	3187[62]	2270	3100
C (J kg^{-1} K^{-1})	128	713	900[62]	673[63]	680	750

This can be rewritten to a corresponding constraint on the aspect ratio of the cantilever,

$$\frac{w}{L} = \frac{1}{t_1 k_1 + t_2 k_2} \frac{\Delta \hat{P}\big|_{\Delta T_\text{base}}}{2\Delta T_\text{base}}, \tag{11}$$

where k_i is the thermal conductivity of the respective layers.

In a similar fashion, the uncertainty in the measured thermal input is limited by the Brownian motion of the cantilever and can be quantified as

$$\Delta \hat{P}_\text{noise} = \frac{2}{\Gamma} \sqrt{\frac{k_\text{B}}{EI}} \frac{w t_2^2}{L\sqrt{L}} \sqrt{T_\text{avg}}. \tag{12}$$

This can be rewritten for the constraint on length and width and their effects on the equivalent thermal noise. For this, either the tip temperature needs to be assumed constant for each cantilever (irrespective of the dimensions) or the incident laser power is assumed constant. Under the assumption that the incident laser spot is small enough to completely fit on the cantilever, a constant laser power is preferred as this makes the optical power reflected to the PSD independent of the cantilever.

Under vacuum conditions with heat added at the free-end of the cantilever, a linear temperature distribution ($T_\text{avg} = \frac{P_\text{abs}}{2G} + T_\text{base}$) results. From Eq. (1) and Eq. (12) in the supplementary material, it then follows that

$$w = \frac{c_1 L^3 - P_\text{abs} L}{c_2}, \tag{13}$$

where P_abs is the absorbed laser power and

$$c_1 = \frac{\Delta \hat{P}\big|_\text{thermal noise}^2 \Gamma^2 h E_1 E_2 K_1 (h k_1 + k_2)}{24 k_\text{B}(h E_1 + E_2)}, \tag{14}$$

$$c_2 = T_\text{base} t_2 (h k_1 + k_2). \tag{15}$$

The equations above describe a set of cantilevers that meet all the thermo-mechanical requirements and constraints. For a high measurement sensitivity, the cantilevers in this set are typically long, slender, and very thin. At the same time, these cantilevers tend to be very compliant and difficult to handle in practice, e.g., during installation into the measurements setup and while gluing spheres to their tips. Therefore, a minimal spring constant of 1 mN m^{-1} is introduced to minimize handling issues. Although significantly more compliant cantilevers[64] are available for scanning probe microscopy, these are typically intended for axial mechanical loading rather than bending. In bending, a spring constant of 1 mN m^{-1} is considered a realistic minimum based on practical experience. This introduces a constraint of the form w/L^3 of

$$\frac{w}{L^3} = \frac{4C(t_1 E_1 + t_2 E_2)}{t_2^3 t_1 E_2 E_1 K_1}. \tag{16}$$

These requirements and constraints are combined in Fig. 8 to form a set of feasible designs. The region of feasible cantilevers is constrained from above by the minimum spring constant (1 mN m^{-1}) and from below by the minimum measurement resolution (100 pW), the thermal noise constraint (5 nW equiv.), and the base temperature uncertainty (1 nW equiv.).
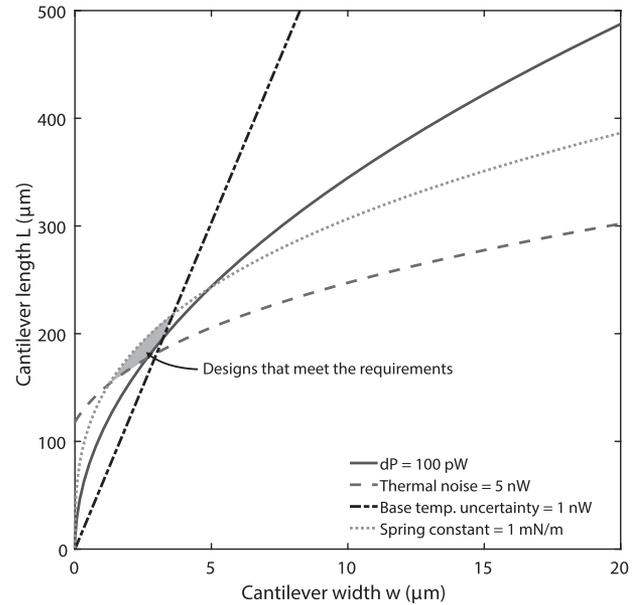
FIG. 8. Required cantilever aspect ratio to meet the design requirements and constraints. The region of feasible designs is constrained from above by the minimum spring constant and from below by the minimum flux resolution, the thermal noise constraint, and the base temperature uncertainty. Results for Al coating on Si$_3$N$_4$, 2 mW incident laser power, 9.3% absorptance, T_base = 298.15 K, and Γ = 5.2 × 10^{-8} m W^{-1}.

C. Selected cantilever dimensions

The cantilever dimensions that follow from the design procedure are listed in Table III under column A. Three additional designs are included with increasing spring constants while performance gets incrementally worse. Figure 9 shows an optical micrograph of the realized cantilevers. The designs are from hereon referred to as cantilevers A–D.

III. BENCHMARKING AGAINST BRUKER MLCT-C

To compare the designed cantilevers to the commercially available alternatives, the results are benchmarked against the Bruker MLCT-C. As explained before, this cantilever and very similar alternatives from other manufacturers were used by other groups for measuring the near-field heat transfer,[32–34,39] making it a relevant benchmark. A micrograph of this probe including its dimensions is shown in Fig. 10.

The thermo-mechanical model presented in Secs. II and III is valid only for a rectangular cantilever with a rectangular cross section and cannot be used directly for the triangular MLCT-C probe. In contrast to Wanders' effective-width method used to evaluate the MLCT-C, the probe is here modeled using a finite element model in COMSOL Multiphysics. This model is used to calculate the temperature gradients and the resulting mechanical deformation. The geometry of the MLCT-C probe, with its two separated legs that are joined in a triangular section at the free-end, causes a non-linear temperature profile along the cantilever length as depicted in Fig. 11.

TABLE III. Nominal dimensions and calculated performance parameters for optimized cantilevers. All cantilevers have a silicon nitride substrate of 309 nm thick and an aluminum reflective coating of 100 nm thick on one side. The resonance frequency f_L is calculated assuming that a 20 μm diameter silica sphere is attached at the free-end.

Parameter	A	B	C	D
Length L (μm)	208	137	112	77
Width w (μm)	3.40	4.50	5.00	4.80
Spring constant C (mN m^{-1})	1.10	5.20	11	31
Conductance G (W K^{-1})	5.30×10^{-7}	1.10×10^{-6}	1.40×10^{-6}	2.00×10^{-6}
Rotation sensitivity $\frac{\partial \theta}{\partial P}$ (W^{-1})	6.90×10^{3}	2.30×10^{3}	1.40×10^{3}	6.70×10^{2}
Deflection sensitivity $\frac{\partial z}{\partial P}$ (m W^{-1})	4.80×10^{-1}	1.00×10^{-1}	5.10×10^{-2}	1.70×10^{-2}
Equivalent thermal noise (equal average temperature) (nW K$^{-1/2}$)	0.27	0.57	0.82	1.40
Equivalent thermal noise (equal absorbed power) (W$^{1/2}$)	3.70×10^{-7}	5.40×10^{-7}	6.90×10^{-7}	9.90×10^{-7}
Thermal time constant (cantilever only) τ (ms)	0.41	0.18	0.12	5.70×10^{-2}
Thermal bandwidth $1/(5\tau)$ (kHz)	0.48	1.10	1.70	3.50
First resonance frequency (no sphere) f_1 (kHz)	11.4	26.3	39.3	83.0
First resonance frequency (with sphere) f_L (kHz)	1.58	3.41	4.87	8.40

In the effective-width method of Wanders, a linear temperature profile is assumed that results in an overestimation of the deflection and rotation sensitivities.

For both the Bruker MLCT-C and the designed cantilevers, the tip temperature, the tip rotation, and the tip deflection were calculated as a function of the heat flux absorbed at the probe tip. The results of these simulations are shown in Fig. 12 and are used to calculate the effective conductances, as well as the sensitivities of rotation and deflection to heat input. Table IV presents a direct comparison between the MLCT-C and the designed cantilever A, the latter of which is 41× more sensitive.

To compare the thermal noise levels of the designs, Eq. (12) is used to calculate the temperature-normalized equivalent thermal noise ($\Delta\hat{P}_{\text{noise}}/\sqrt{T_{\text{avg}}}$) (integrated over all frequencies). This probe parameter can be used to estimate the equivalent thermal noise (expressed in the measured flux) for equal average temperatures. It is estimated at 2.3 nW K$^{-1/2}$ and 0.27 nW K$^{-1/2}$ for the MLCT-C and the designed cantilever A, respectively. However, at equal levels of absorbed heat from the OBD laser, the average temperature varies between the designs. Because the average temperature is inversely proportional to the conductance G, the previous metric can be multiplied by $\sqrt{1/G}$ for a metric that allows comparison

at equal levels of absorbed power. The values of this metric are 1.5×10^{-6} W$^{1/2}$ and 3.7×10^{-7} W$^{1/2}$ for the MLCT-C and cantilever A, respectively. Cantilever A performs 4.1× better than the MLCT-C in terms of equivalent thermal noise at equal levels of absorbed power. The signal-to-noise ratio can thus be improved by a factor of 168 compared to the benchmark.

To verify the theoretical model, the optimized cantilever is also modeled using the same multiphysics finite element method (FEM). The sensitivities derived using the analytical model and the
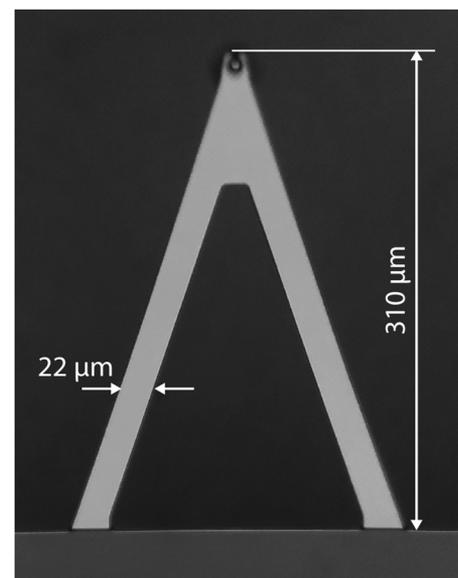
FIG. 10. Micrograph of the Bruker MLCT-C probes with specified dimensions. The probe consists of a 0.55 μm thick silicon nitride substrate, a 40 nm thick gold reflective coating, and a 5 nm thick titanium adhesion layer. All dimensions used in the finite element model were measured relative to the dimensions indicated in the micrograph.

FIG. 9. Optical micrograph of the manufactured cantilevers, labeled according to Table III. The square on the right labeled CAL is used for measuring the optical properties of the cantilevers and has the same layer thicknesses as the probes.
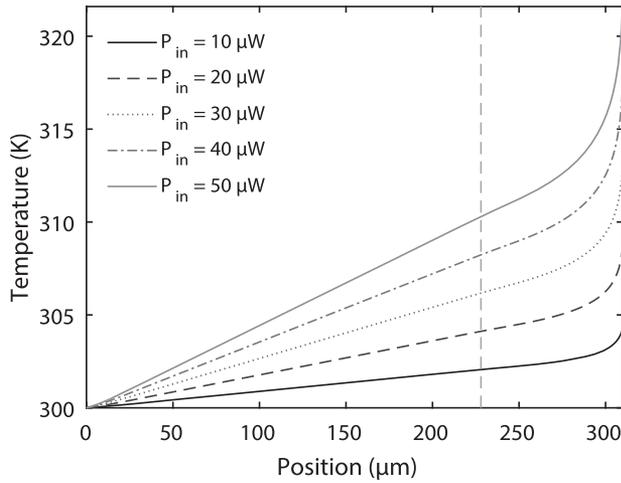
FIG. 11. Temperature profiles for the Bruker MLCT-C probes. The temperature at the clamped-end is kept constant at 300 K. The mentioned power values represent the heating power absorbed by the cantilever, not the incident power. The vertical line indicates the location where the two legs are joined and form a triangle from thereon to the free-end. The 5 nm Ti adhesion layer is ignored.

IV. EXPERIMENTAL VALIDATION

To validate the design, the cantilevers are manufactured and the sensitivities are measured indirectly.

A. Cantilever manufacturing

The manufacturing of the cantilevers starts on a standard 380 μm thick (100) silicon wafer. A 315 nm thick silicon-rich nitride (SiRN) layer is deposited by Low Pressure Chemical Vapor Deposition (LPCVD). The deposited SiRN layer is then patterned using Reactive Ion Etching (RIE) to define the cantilevers. A second patterning step is employed to etch through the silicon wafer by Deep Reactive Ion Etching (DRIE). After the DRIE process, the cantilevers are released by wet chemical etching of silicon in tetramethylammonium hydroxide (TMAH). After release, a 100 nm thick aluminum layer is sputtered on one side to form the reflective coating. These steps are illustrated in Fig. 13.

In the design, the reflective coating is assumed to be perfectly flat. The scattering of light caused by the surface roughness, however, affects the reflectance of the probe. This effect is modeled using the simple model presented by Bennet and Porteus.[65] The specular reflectance R is calculated from the ideal reflectance R_0 under normal incidence as

$$R = R_0 \left(\exp\left(-\frac{4\pi\sigma^2}{\lambda^2}\right) + \frac{2^5\pi^4}{m^2}\left(\frac{\sigma}{\lambda}\right)^4 \Delta\theta^2 \right), \quad (17)$$

where σ is the root-mean-square surface roughness, λ is the wavelength of the light, m is the root-mean-square slope of the surface, and $\Delta\theta$ is the acceptance angle of the optics. The right-hand side term vanishes quickly with larger λ, and the reflectance is approximated as

$$R \approx R_0 \exp\left(-\frac{4\pi\sigma^2}{\lambda^2}\right). \quad (18)$$

Figure 14 shows this relation in dimensionless form. A root-mean-square roughness of 3% or less of the wavelength limits the difference between ideal and non-ideal specular reflections to 1%. For a wavelength of 635 nm, the relative roughness translates to a root-mean-square roughness of 19 nm.

sensitivities derived using the FEM are in very good agreement with each other, with a maximum difference of less than 1%. The differences in conductance and spring constant are 6% and 3%, respectively, and are considered in adequate agreement for this discussion. The difference in the conductance values calculated using the analytical model and using the FEM can be attributed to the assumption of one-dimensional heat flow in the theoretical model and thus the lack of interaction between the layers. Similarly, the difference for the spring constant values using both models can be attributed to the lack of the Poisson effect in the theoretical model.
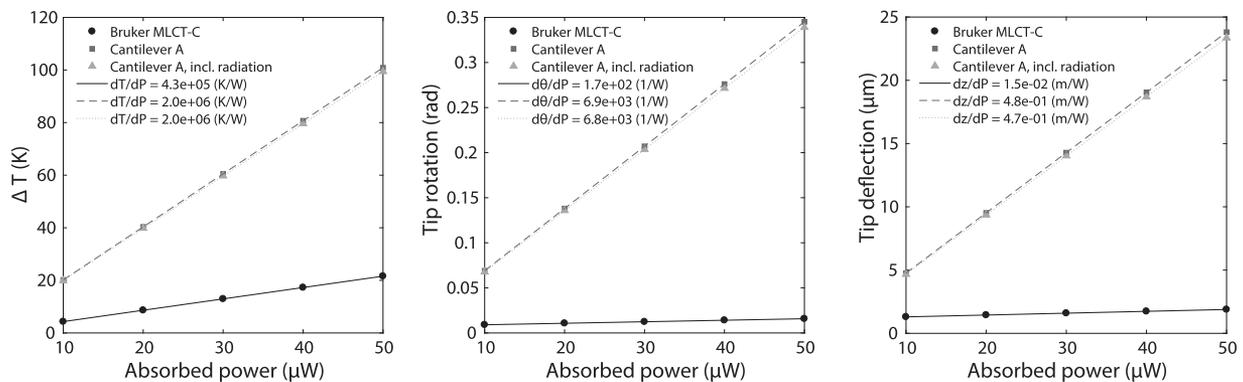
FIG. 12. Temperature gradients (left), tip rotation (center), and tip deflection (right) for various levels of absorbed heat flux at the cantilever tip.

TABLE IV. Comparison of the performance of the Bruker MLCT-C probe based on the finite element method (FEM) and the optimized probes. The table also includes a comparison between the results obtained from the theoretical model, a FEM model that only includes conduction, and a FEM model taking into account both conduction via the probe and radiative heat losses to the environment. The relative performance is calculated as that of the optimized probe (FEM) relative to that of the Bruker MLCT-C. *Nota bene*: the spring constant calculated for the MLCT-C probe is higher than the nominal spring constant of 10 mN m^{-1} specified by Bruker but is within the specified range of 5 mN m^{-1} to 20 mN m^{-1}.

Parameter	Bruker MLCT-C	Optimized (FEM)	Optimized (theory)	Optimized (FEM + losses)	Relative performance
Conductance G (W K^{-1})	2.3×10^{-6}	5.00×10^{-7}	5.30×10^{-7}	5.00×10^{-7}	2.10×10^{-1}
Rotation sensitivity $\partial\theta/\partial P$ (rad W^{-1})	1.70×10^{2}	6.90×10^{3}	6.90×10^{3}	6.80×10^{3}	4.10×10^{1}
Deflection sensitivity $\partial z/\partial P$ (m W^{-1})	1.50×10^{-2}	4.80×10^{-1}	4.80×10^{-1}	4.70×10^{-1}	3.30×10^{1}
Spring constant C (N m^{-1})	1.60×10^{-2}	1.10×10^{-3}	1.10×10^{-3}	1.10×10^{-3}	. . .
Equivalent thermal noise at equal average temperature (nW K$^{-1/2}$)	2.3	0.27	0.27	0.27	8.5
Equivalent thermal noise at equal absorbed power (W$^{1/2}$)	1.50×10^{-6}	3.70×10^{-7}	3.70×10^{-7}	3.70×10^{-7}	4.10

The surface roughness of three chips (each with five cantilevers) was measured using a Park XE7 atomic force microscope and BudgetSensors SHR300 probes (1 nm tip radius) over a 1 μm × 1 μm area to be 3.4 nm ± 0.4 nm root-mean-square. The realized probes are thus smooth enough for scattering to be considered a minor contributor to the optical absorptance and reflectance values.

B. Measuring the cantilever sensitivity

To validate the design procedure, the sensitivity of the realized probes is measured under high vacuum conditions. The sensitivity of the probe cannot be measured directly and needs to be derived from measurable quantities using

$$\frac{\partial\theta}{\partial P_{\text{abs}}} = \frac{\partial X_{\text{P}}}{\partial P_{\text{abs}}}\left(\frac{\partial X_{\text{P}}}{\partial x}\frac{\partial x}{\partial\theta}\right)^{-1}. \qquad (19)$$

The absorbed power is calculated from the incident power and the absorptance, which is measured separately (see the supplementary

material for details). The sensitivity $\partial X_{\text{P}}/\partial x$ is measured by displacing the PSD by controlled amounts with respect to the reflected beam and the rest of the system in steady-state. Unfortunately, the sensitivity $\frac{\partial x}{\partial\theta}$ cannot be measured directly in the available system, but it is estimated at (99.6 ± 3.0) mm rad^{-1} (see the supplementary material for details of this estimation).

The measured sensitivities are summarized in Table V. For cantilevers B, C, and D, the measured sensitivities are close to their designed values. The differences can be explained by the measurement uncertainty and the loss of sensitivity due to measuring not at the very tip of the probes but slightly behind them. As is shown in the supplementary material, the actual sensitivity of the probe depends on the position of the laser spot along the length of the probe and the spot size. This causes the realized sensitivity to drop to a level between 55% and 90% of the theoretical sensitivity. If these effects
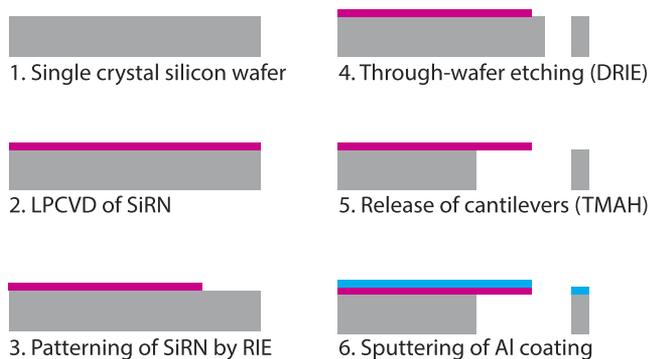
FIG. 13. The cantilevers are manufactured in a six step process starting from a standard (100) silicon wafer. Silicon-rich nitride is deposited on top, and the cantilevers are defined using (deep) reactive ion etching (RIE). After release using TMAH, an aluminum coating is sputtered on top.
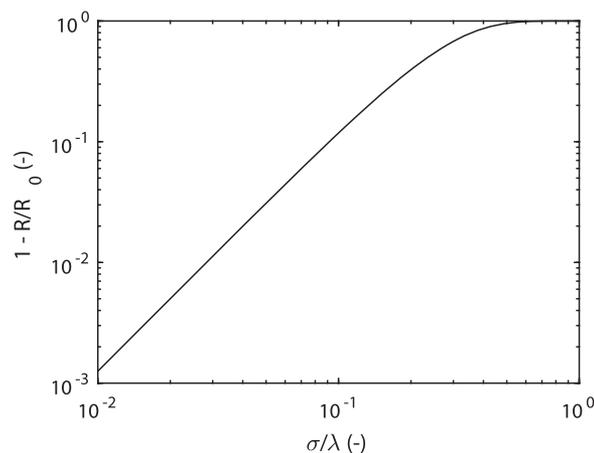
FIG. 14. Relative error in specular reflectance ($1 - R/R_0$) under normal incidence and as a function of the root-mean-square surface roughness σ relative to the wavelength λ.

TABLE V. Measured sensitivities and derived probe sensitivity.

Parameter	Cantilever A	Cantilever B	Cantilever C	Cantilever D
$\partial \bar{X}_p / \partial I$ (mA^{-1})	1.58 ± 0.0706	1.12 ± 0.0738	0.217 ± 0.0418	0.143 ± 0.00872
$\partial P_{abs} / \partial I$ (μW mA^{-1})	$3.43 \pm 1.48 \times 10^{-1}$	$3.42 \pm 2.12 \times 10^{-1}$	$3.29 \pm 5.53 \times 10^{-1}$	$2.64 \pm 1.55 \times 10^{-1}$
$\partial \bar{X}_p / \partial x$ (m^{-1})	906 ± 64	1220 ± 39	594 ± 106	815 ± 48
$\partial x / \partial \theta$ (mm rad^{-1})[a]	99.6 ± 3.0	99.6 ± 3.0	99.6 ± 3.0	99.6 ± 3.0
$\partial \theta / \partial P_{abs}$ (rad W^{-1})[b]	$5.08 \times 10^3 \pm 503$[c]	$2.70 \times 10^3 \pm 272$	$1.12 \times 10^3 \pm 355$	669 ± 101
$\partial \theta / \partial P_{abs}$ (rad W^{-1}), theory	6.90×10^3	2.30×10^3	1.40×10^3	6.70×10^2

[a]By design, theoretical value. See Section V of the supplementary material.
[b]Calculated from the other sensitivities.
[c]Micrographs show local damage to the cantilever that is likely caused by excessive heating. Some samples had broken, while others were discolored locally, which indicates changes in the optical properties.

are incorporated into the theoretical relations, however, the advantage of using theoretical relations for design purposes is lost due to the complexity and length of the equations.

Cantilever A is the most sensitive of the four designs, but the measured sensitivity differs significantly from the designed value. Optical micrographs and scanning electron micrographs (see the supplementary material) showed significant damage to the cantilever coating after calibration, which is probably caused by excessive heating. This unforeseen effect was not observed in the other designs due to their higher thermal conductance and lower maximum temperatures. It is hypothesized that the deviation from the design value in this case can be traced to the sensitivity changing over time due to the sustained damage.

Attempts to measure the sensitivity of the Bruker MLCT-C cantilever were unreliable due to large variations in the measured absorptance. For the MLCT-C, h is smaller than 0.10 with a coating thickness of 40 nm and a total thickness of 0.55 μm. As is clear from Fig. 3, large fluctuations in absorptance are expected with small variations in thickness for this combination of the coating thickness and thickness ratio. The absorptance ranges from 4.5% to 8.5% in a ±5 nm interval around the nominal coating thickness. Using this range for the absorptance, the sensitivity is estimated between 337 rad W^{-1} to 562 rad W^{-1}, which is significantly higher than that estimated from the finite element model. Because the processing conditions are unknown, it is likely that the effective material properties and layer thicknesses vary from those assumed in the theoretical model. This is also reflected in the stiffness range specified by the manufacturer, which ranges from 5 mN m^{-1} to 20 mN m^{-1}.

V. DISCUSSION

A. Limited speed of measurement

It is important to note that the cantilever dimensions and materials also influence the dynamics of the probe, which are directly linked to the speed of measurement that can be attained on a system level. When the speed of measurement becomes a driving parameter, for example, for microscopy applications, these influences on the cantilever dynamics will have to be considered in the design of the probe. To study the influence of the design parameters on the speed of measurement, the first mechanical resonance frequency and the characteristic thermal time constant are determined. These are used

as first order estimates of the response time to a thermal load at the free-end of the cantilever.

The majority of near-field heat transfer measurements are conducted under vacuum conditions. Therefore, contributions from mechanical or aerodynamic damping and heat transfer to the environment are neglected here. For a cantilever with a sphere attached to its free-end, the first mechanical resonance frequency can then be estimated as[66]

$$f_L \approx \frac{1}{2\pi} \sqrt{\frac{3EI}{(0.24\,m + M)L^3}}, \tag{20}$$

where m is the mass of the cantilever and M is the mass of the sphere. According to Barnes *et al.*,[40] the thermal response time for a heat load at the free-end of the cantilever can be estimated as

$$\tau = \frac{1}{D} \frac{L^3}{3}, \tag{21}$$

where the thermal diffusivity D for the bilayer structure is equal to[67]

$$D = \frac{k_1 t_1 + k_2 t_2}{c_{p_1} \rho_1 t_1 + c_{p_2} \rho_2 t_2}. \tag{22}$$

Because 99.4% of the total temperature change is achieved after 5τ has passed, the thermal bandwidth of the cantilever is defined as

$$f_{T,\,cant.} = \frac{1}{5\tau}. \tag{23}$$

However, the microsphere plays a significant role in the thermal bandwidth. Using a lumped parameter model of the sphere that approximates the sphere as a cylindrical conductor of thermal conductance G and radius R, its thermal time constant can be estimated to first order as

$$\tau_{sphere} \approx \frac{mc}{G} \approx \frac{8\rho c R^2}{3k}. \tag{24}$$

For a glass sphere, $\log_{10}(f_T) \approx -7 - 2\log_{10}(R)$, which yields a wide range of $f_R \approx 1 \times 10^{11}$ Hz to $f_T \approx 10$ Hz for $R = 1$ nm and $R = 100$ μm, respectively.

Table III lists the first resonance frequency for a probe with no sphere attached, the resonance frequency with a sphere attached, the thermal time constant, and the thermal bandwidth. The glass microsphere has a diameter of 20 μm. Although the addition of the sphere

reduces the mechanical resonance frequency by $7 - 10\times$, the thermal response time remains the limiting factor for the achievable measurement speed. In the case of cantilever A, the thermal measurement bandwidth of the cantilever itself is 483 Hz, while that of the sphere is 534 Hz.

The thermal response time of the probe (consisting of a cantilever with an attached sphere) can only be improved by using a smaller sphere and a smaller cantilever and at the cost of measurement sensitivity.

B. The effect of ignoring radiative losses

In the analysis above and in the analytical model, the contribution of radiative heat transfer between the cantilever and its surroundings is considered to be negligible. To confirm the validity of this assumption, the thermal and thermo-mechanical response of the designed cantilever probe are modeled using a finite element method in which heat transfer to the environment via black-body radiation is included. The clamped-end of the probe is kept at a constant temperature of 300 K, while a constant flux of 10 μW–50 μW is absorbed at its free-end. The environment is set at a constant temperature of 293.15 K and at a perfect vacuum. The emissivity of all radiating surfaces is set at an unrealistically high, worst-case value of 1. At the highest power setting of the laser diode, the tip temperature of the probe does not exceed 400 K. The magnitude of the temperature gradients, the tip rotation, and the tip deflection are shown in Fig. 12. The corresponding sensitivities are summarized in Table IV. Ignoring radiative heat losses introduces an error of less than 1.5% in the conductance and less than 1.8% in the sensitivities. At these temperatures, radiative losses are thus negligible for design purposes.

For a worst-case estimation of the radiative heat losses, the cantilever is assumed to take a uniform temperature distribution equal to the maximum tip-temperature. The corresponding loss is

$$q_{\text{rad. loss}} = \sigma A_{\text{rad}} \epsilon \left(T_{\text{tip}}^4 - T_{\text{env}}^4 \right), \quad (25)$$

where $\sigma = 5.67 \times 10^{-8}$ W m^{-2} K^{-1} is the Stefan-Boltzmann constant, $A_{\text{rad}} \approx 1.6 \times 10^{-9}$ m^2 is the total radiating area, $\epsilon = 1$ is the (assumed worst-case) effective emissivity, $T_{\text{tip}} = 400$ K is the tip temperature, and $T_{\text{env}} = 293.15$ K is the temperature of the environment. From this, it follows that the thermal flux ≤ 1.6 μW, which is small in comparison to the power absorbed from the incident laser. The change in radiative losses due to a change in the temperature of the environment is estimated as

$$\frac{\partial q_{\text{rad. loss}}}{\partial T_{\text{env}}} = -4\sigma A_{\text{rad}} \epsilon T_{\text{env}}^3 \quad (26)$$

and amounts to ~9.1 nW K^{-1}. In practice, the temperature variation inside the vacuum chamber is between 50 mK and 100 mK over the course of a day, which reduces the effect of radiative losses to less than 1 nW. This is a small contributor to the drift at the system level that is dominated by the drift of the laser power in the order of 50 nW in absorbed power.

C. The effect of ambient pressure

In the theoretical discussion, vacuum conditions were assumed and the effects of convective and conductive heat losses to the environment were ignored. Additional loss of heat to the environment via heat transfer to the ambient air results in a reduced temperature gradient along the length of the cantilever.[68] This results in a reduced mismatch strain between the layers for an equal thermal input at the cantilever tip and thus a reduction in the sensitivity. Convective heat transfer at micrometer length scales is currently not well understood, and experimental evidence suggests convective heat transfer coefficients ranging from 30 W m^{-2} K^{-1} to 10 kW m^{-2} K^{-1} at ambient pressure (see Ref. 67 and the references therein). This makes it difficult to quantify the reduction in sensitivity with any reasonable degree of certainty.

However, experimental evidence provided by Lee et al.[69] suggests that convective losses can be ignored for Knudsen numbers larger than 10. The Knudsen number is the ratio between the mean-free path length in the gas and the physical length scale of the object. For the dimensions of the cantilevers that are presented here, no appreciable pressure effects on the sensitivity are expected for pressures below 0.1 mbar. The experiments are conducted at pressures between 1×10^{-7} mbar and 1×10^{-6} mbar (see the supplementary material for details) to eliminate the effects of gas conduction between the sphere and the substrate. Pressure effects on the probe sensitivity can therefore safely be ignored.

D. The effect of Casimir and Van der Waals forces

When the probe approaches the sample, Casimir and Van der Waals forces will be exerted on the sphere. These forces increase with diminishing separation. At very small distances (≤ 10 nm), the sum of these forces can be estimated[70] using

$$F \approx \frac{A_{\text{H}} R}{6d^2}, \quad (27)$$

where A_{H} is Hamaker's constant (6.35×10^{-20} J for silica particles in vacuum[71]), R is the radius of the sphere, and d is the separation. Because the sphere is not fixed in line with the cantilever, a torque is applied to the cantilever with an effective arm of length R. The equivalent thermal input can be expressed as

$$\hat{P}_{\text{vdW}} = \frac{\partial P}{\partial \theta} \Delta \theta = \frac{\partial P}{\partial \theta} \frac{1}{2} \frac{A_{\text{H}} R^2}{C d^2 L^2}, \quad (28)$$

where C is the spring constant in bending of the cantilever. At a separation of 10 nm, this equates to 97 nW for cantilever A with a sphere 20 μm diameter sphere attached to its tip. It quickly diminishes to less than 1 nW for a separation of 100 nm. Although these forces are fairly small, they easily exceed other contributions at small separations. They can, however, be compensated for by measuring the spurious forces separately when the tip temperature and substrate temperature are equal. For this, the substrate temperature needs to be raised.

VI. CONCLUSIONS

Near-field radiative heat transfer measurements benefit from probes that are designed for that specific purpose. Using a relatively simple analytical model, a family of feasible cantilever designs that are constrained in terms of resolution, thermal noise, temperature drift, and bending stiffness was derived. The model considers the cantilever as an integral part of the measurement system, and the effects of design decisions are evaluated considering system level performance.

The theoretical model used for this design matches well with the finite element model. The analytical model can be improved by incorporating the exchange of heat between the layers and the effects of finite spot size for the incident light. This will, however, result in theoretical relations that are no longer tangible for design purposes because of their complexity and their length.

This paper showed theoretically and experimentally that under realistic design constraints, the designed probes are up to 41 times more sensitive than the benchmark. This was achieved by limiting the thermal conductance while maintaining a large difference in thermal expansion coefficients between the two layers. In practice, the performance of the cantilever probes was limited by damage that was possibly sustained from carbon contamination. Future work will have to consider these practical effects if performance is to be further improved. Furthermore, for practical applications in scanning probe microscopy, the measurement speed is an important parameter that was omitted from the design in this paper. The microsphere plays an important role in the attainable measurement bandwidth and will have to be incorporated in the design process if dynamic system performance is to be further improved.

SUPPLEMENTARY MATERIAL

See the supplementary material for more in-depth derivations of the analytical model, the methods used for measuring the reflectance and absorptance of the cantilevers, an estimation of the uncertainty of the beam displacement due to de-focus in the optical beam deflection system, an analytical treatise of the cantilever sensitivity under finite spot size, and a treatise of the found damage to the cantilevers of design A.

ACKNOWLEDGMENTS

DATA AVAILABILITY

The data that support the findings of this study are available from the corresponding author upon reasonable request.

REFERENCES

[1]C. M. Hargreaves, "Anomalous radiative transfer between closely-spaced bodies," Phys. Lett. A **30**(9), 491–492 (1969).

[2]S. M. Rytov, *Theory of Electrical Fluctuations and Thermal Radiation* (Izd-vo Akademiia Nauk S.S.S.R., Moscow, 1953).

[3]S. M. Rytov, "Theory of electric fluctuations and thermal radiation," Series AFCRC-TR-59-162, Electronics Research Directorate, Air Force Cambridge Research Center, Air Research and Development Command, U.S. Air Force, Moscow, 1st ed., 1959.

[4]D. Polder and M. Van Hove, "Theory of radiative heat transfer between closely spaced bodies," Phys. Rev. B **4**(10), 3303–3314 (1971).

[5]E. G. Cravalho, C. L. Tien, and R. P. Caren, "Effect of small spacings on radiative transfer between two dielectrics," J. Heat Transfer **89**(4), 351 (1967).

[6]E. Cravalho, G. Domoto, and C. Tien, "Measurements of thermal radiation of solids at liquid-helium temperatures," in *3rd Thermophysics Conference* (American Institute of Aeronautics and Astronautics, Reston, VA, 1968), pp. 531–542.

[7]R. S. DiMatteo, P. Greiff, S. L. Finberg, K. A. Young-Waithe, H. K. H. Choy, M. M. Masaki, and C. G. Fonstad, "Enhanced photogeneration of carriers in a semiconductor via coupling across a nonisothermal nanoscale vacuum gap," Appl. Phys. Lett. **79**(12), 1894–1896 (2001).

[8]X. J. Hu, A. Jain, and K. E. Goodson, "Investigation of the natural convection boundary condition in microfabricated structures," Int. J. Therm. Sci. **47**(7), 820–824 (2008).

[9]R. S. Ottens, V. Quetschke, S. Wise, A. A. Alemi, R. Lundock, G. Mueller, D. H. Reitze, D. B. Tanner, and B. F. Whiting, "Near-field radiative heat transfer between macroscopic planar surfaces," Phys. Rev. Lett. **107**(1), 014301 (2011).

[10]T. Kralik, P. Hanzelka, M. Zobac, M. Vera, T. Fort, and M. Horak, "Strong near-field enhancement of radiative heat transfer between metallic surfaces," Phys. Rev. Lett. **109**(22), 224302 (2012).

[11]S. Sadat, E. Meyhofer, and P. Reddy, "Resistance thermometry-based picowatt-resolution heat-flow calorimeter," Appl. Phys. Lett. **102**(16), 163110 (2013).

[12]R. St-Gelais, B. Guha, L. Zhu, S. Fan, and M. Lipson, "Demonstration of strong near-field radiative heat transfer between integrated nanostructures," Nano Lett. **14**(12), 6971–6975 (2014).

[13]T. Ijiro and N. Yamada, "Near-field radiative heat transfer between two parallel SiO$_2$ plates with and without microcavities," Appl. Phys. Lett. **106**(2), 023103 (2015).

[14]K. Ito, A. Miura, H. Iizuka, and H. Toshiyoshi, "Parallel-plate submicron gap formed by micromachined low-density pillars for near-field radiative heat transfer," Appl. Phys. Lett. **106**(8), 083504 (2015).

[15]B. Song, Y. Ganjeh, S. Sadat, D. Thompson, A. Fiorino, V. Fernández-Hurtado, J. Feist, F. J. Garcia-Vidal, J. C. Cuevas, P. Reddy, and E. Meyhofer, "Enhancement of near-field radiative heat transfer using polar dielectric thin films," Nat. Nanotechnol. **10**, 253–258 (2015).

[16]B. Song, D. Thompson, A. Fiorino, Y. Ganjeh, P. Reddy, and E. Meyhofer, "Radiative heat conductances between dielectric and metallic parallel plates with nanoscale gaps," Nat. Nanotechnol. **11**(6), 509–514 (2016).

[17]R. St-Gelais, L. Zhu, S. Fan, and M. Lipson, "Near-field radiative heat transfer between parallel structures in the deep subwavelength regime," Nat. Nanotechnol. **11**(6), 515–519 (2016).

[18]K. Ito, K. Nishikawa, A. Miura, H. Toshiyoshi, and H. Iizuka, "Dynamic modulation of radiative heat transfer beyond the blackbody limit," Nano Lett. **17**, 4347–4353 (2017).

[19]D. Thompson, L. Zhu, R. Mittapally, S. Sadat, Z. Xing, P. McArdle, M. M. Qazilbash, P. Reddy, and E. Meyhofer, "Hundred-fold enhancement in far-field radiative heat transfer over the blackbody limit," Nature **561**(7722), 216–221 (2018).

[20]A. Fiorino, D. Thompson, L. Zhu, B. Song, P. Reddy, and E. Meyhofer, "Giant enhancement in radiative heat transfer in sub-30 nm gaps of plane parallel surfaces," Nano Lett. **18**(6), 3711–3715 (2018).

[21]J. DeSutter, L. Tang, and M. Francoeur, "A near-field radiative heat transfer device," Nat. Nanotechnol. **14**(8), 751–755 (2019).

[22]L. Zhu, A. Fiorino, D. Thompson, R. Mittapally, E. Meyhofer, and P. Reddy, "Near-field photonic cooling through control of the chemical potential of photons," Nature **566**(7743), 239–244 (2019).

[23]H. Salihoglu, W. Nam, L. Traverso, M. Segovia, P. K. Venuthurumilli, W. Liu, Y. Wei, W. Li, and X. Xu, "Near-field thermal radiation between two plates with sub-10 nm vacuum separation," Nano Lett. **20**(8), 6091–6096 (2020).

[24]X. Ying, P. Sabbaghi, N. Sluder, and L. Wang, "Super-planckian radiative heat transfer between macroscale surfaces with vacuum gaps down to 190 nm directly created by SU-8 posts and characterized by capacitance method," ACS Photonics **7**(1), 190–196 (2020).

[25]C. C. Williams and H. K. Wickramasinghe, "Scanning thermal profiler," Appl. Phys. Lett. **49**(23), 1587 (1986).

[26] J. B. Xu, K. Läuger, R. Möller, K. Dransfeld, and I. H. Wilson, "Heat transfer between two metallic surfaces at small distances," J. Appl. Phys. **76**(11), 7209 (1994).

[27] W. Müller-Hirsch, A. Kraft, M. T. Hirsch, J. Parisi, and A. Kittel, "Heat transfer in ultrahigh vacuum scanning thermal microscopy," J. Vac. Sci. Technol. A **17**(4), 1205 (1999).

[28] A. Kittel, W. Müller-Hirsch, J. Parisi, S.-A. Biehs, R. Daniel, and M. Holthaus, "Near-field heat transfer in a scanning thermal microscope," Phys. Rev. Lett. **95**(22), 224301 (2005).

[29] U. F. Wischnath, J. Welker, M. Munzel, and A. Kittel, "The near-field scanning thermal microscope," Rev. Sci. Instrum. **79**, 073708 (2008).

[30] K. Kloppstech, N. Könne, S.-A. Biehs, A. W. Rodriguez, W. Ludwig, D. Hellmann, and A. Kittel, "Giant heat transfer in the crossover regime between conduction and radiation," Nat. Commun. **8**, 14475 (2017).

[31] L. Cui, W. Jeong, V. Fernández-Hurtado, J. Feist, F. J. García-Vidal, J. C. Cuevas, E. Meyhofer, and P. Reddy, "Study of radiative heat transfer in Ångström- and nanometre-sized gaps," Nat. Commun. **8**, 14479 (2017).

[32] A. Narayanaswamy, S. Shen, and G. Chen, "Near-field radiative heat transfer between a sphere and a substrate," Phys. Rev. B **78**(11), 115303 (2008).

[33] E. Rousseau, A. Siria, G. Jourdan, S. Volz, F. Comin, J. Chevrier, and J.-J. Greffet, "Radiative heat transfer at the nanoscale," Nat. Photonics **3**(9), 514–517 (2009).

[34] S. Shen, A. Narayanaswamy, and G. Chen, "Surface phonon polaritons mediated energy transfer between nanoscale gaps," Nano Lett. **9**(8), 2909–2913 (2009).

[35] P. J. van Zwol, L. Ranno, and J. Chevrier, "Tuning near field radiative heat flux through surface excitations with a metal insulator transition," Phys. Rev. Lett. **108**(23), 234301 (2012).

[36] F. Menges, M. Dittberner, L. Novotny, D. Passarello, S. S. P. Parkin, M. Spieser, H. Riel, and B. Gotsmann, "Thermal radiative near field transport between vanadium dioxide and silicon oxide across the metal insulator transition," Appl. Phys. Lett. **108**(17), 171904 (2016).

[37] P. L. Sambegoro, "Experimental investigations on the influence of curvature and materials on near-field thermal radiations," Doctoral dissertation (Massachusetts Institute of Technology, 2016).

[38] G. Meyer and N. M. Amer, "Novel optical approach to atomic force microscopy," Appl. Phys. Lett. **53**(12), 1045 (1988).

[39] R. M. Wanders, "Near field thermal radiation distance sensing," MS thesis(TNO/TU Delft, Delft, 2014), available at http://resolver.tudelft.nl/uuid:6a72c53f-299d-4ded-b78f-ee7990c2adb

[40] J. R. Barnes, R. J. Stephenson, C. N. Woodburn, S. J. O'Shea, M. E. Welland, T. Rayment, J. K. Gimzewski, and Ch. Gerber, "A femtojoule calorimeter using micromechanical sensors," Rev. Sci. Instrum. **65**(12), 3793 (1994).

[41] J. Lai, T. Perazzo, Z. Shi, and A. Majumdar, "Optimization and performance of high-resolution micro-optomechanical thermal sensors," Sens. Actuators, A **58**(2), 113–119 (1997).

[42] C. Canetta and A. Narayanaswamy, "Sub-picowatt resolution calorimetry with a bi-material microcantilever sensor," Appl. Phys. Lett. **102**(10), 103112 (2013).

[43] P. E. Rutten, "High speed two-dimensional optical beam position detector," Rev. Sci. Instrum. **82**(7), 073705 (2011).

[44] B. Harbecke, "Coherent and incoherent reflection and transmission of multilayer structures," Appl. Phys. B **39**(3), 165–170 (1986).

[45] S. J. Byrnes, *Multilayer Optical Calculations*, arxiv.org/abs/1603.02720

[46] P. B. Johnson and R. W. Christy, "Optical constants of the noble metals," Phys. Rev. B **6**(12), 4370–4379 (1972).

[47] M. N. Polyanskiy, Refractive Index Database.

[48] A. D. Rakić, "Algorithm for the determination of intrinsic optical constants of metal films: Application to aluminum," Appl. Opt. **34**(22), 4755 (1995).

[49] D. E. Aspnes and A. A. Studna, "Dielectric functions and optical parameters of Si, Ge, GaP, GaAs, GaSb, InP, InAs, and InSb from 1.5 to 6.0 eV," Phys. Rev. B **27**(2), 985–1009 (1983).

[50] Filmetrics. Refractive Index of Si3N4, Silicon Nitride, SiN, SiON.

[51] I. H. Malitson, "Interspecimen comparison of the refractive index of fused silica," J. Opt. Soc. Am. **55**(10), 1205 (1965).

[52] Filmetrics, Refractive Index of SiC, Silicon Carbide, 2018.

[53] A. Abazari, S. Safavi, G. Rezazadeh, and L. Villanueva, "Modelling the size effects on the mechanical properties of micro/nano structures," Sensors **15**(11), 28543–28562 (2015).

[54] H. S. Marnani, "Mechanics of ultra-sensitive nanoelectromechanical silicon cantilevers: A combined experimental-theoretical approach," Doctoral dissertation (Delft University of Technology, 2010).

[55] MatWeb. Gold, Au.

[56] MatWeb. Silicon, Si.

[57] MatWeb. Aluminium, Al.

[58] B. El-Kareh, *Fundamentals of Semiconductor Processing Technology* (Springer US, Boston, MA, 1995).

[59] Accuratus. Silicon Carbide, SiC Ceramic Properties, 2013.

[60] A. Khan, J. Philip, and P. Hess, "Young's modulus of silicon nitride used in scanning force microscope cantilevers," J. Appl. Phys. **95**(4), 1667–1672 (2004).

[61] K. B. Gavan, H. J. R. Westra, E. W. J. M. van der Drift, W. J. Venstra, and H. S. J. van der Zant, "Size-dependent effective Young's modulus of silicon nitride cantilevers," Appl. Phys. Lett. **94**(23), 233108 (2009).

[62] MEMSnet. Material: Silicon Nitride (Si3N4).

[63] AZO Materials, Silicon Nitride (Si3N4) Properties and Applications.

[64] J. A. Vicary, A. Ulcinas, J. K. H. Hörber, and M. Antognozzi, "Micro-fabricated mechanical sensors for lateral molecular-force microscopy," Ultramicroscopy **111**(11), 1547–1552 (2011).

[65] H. E. Bennett and J. O. Porteus, "Relation between surface roughness and specular reflectance at normal incidence," J. Opt. Soc. Am. **51**(2), 123 (1961).

[66] E. Macho-Stadler, M. J. Elejalde-García, and R. Llanos-Vázquez, "Oscillations of end loaded cantilever beams," Eur. J. Phys. **36**(5), 055007 (2015).

[67] R. Bijster, J. de Vreugd, and H. Sadeghian, "Dynamic characterization of bimaterial cantilevers," in *SENSORDEVICES 2013, The Fourth International Conference on Sensor Device Technologies and Applications*, edited by S. Yurish and F. Pacull (IARIA, Barcelona, Spain, 2013), pp. 1–8.

[68] M. Toda, T. Ono, F. Liu, and I. Voiculescu, "Evaluation of bimaterial cantilever beam for heat sensing at atmospheric pressure," Rev. Sci. Instrum. **81**(5), 055104 (2010).

[69] J. Lee, T. L. Wright, M. R. Abel, E. O. Sunden, A. Marchenkov, S. Graham, and W. P. King, "Thermal conduction from microcantilever heaters in partial vacuum," J. Appl. Phys. **101**(1), 014906 (2007).

[70] G. Palasantzas, P. J. van Zwol, and J. T. M. De Hosson, "Transition from Casimir to van der Waals force between macroscopic bodies," Appl. Phys. Lett. **93**(12), 121914 (2008).

[71] L. Bergström, "Hamaker constants of inorganic materials," Adv. Colloid Interface Sci. **70**, 125–169 (1997).